



Article

Engineering Atomic-to-Nano Scale Structural Homogeneity towards High Corrosion Resistance of Amorphous Magnesium-Based Alloys

Yuan Qin ^{1,†}, Wentao Zhang ^{1,†}, Kanghua Li ^{1,†}, Shu Fu ¹, Yu Lou ¹, Sinan Liu ¹, Jiacheng Ge ¹, Huiqiang Ying ¹, Wei-Di Liu ², Xiaobing Zuo ³, Jun Shen ⁴, Shao-Chong Wei ⁵, Horst Hahn ⁶, Yang Ren ⁷, Zhenduo Wu ⁸, Xun-Li Wang ^{7,8}, He Zhu ^{1,*} and Si Lan ^{1,8,9,*}

- ¹ Herbert Gleiter Institute of Nanoscience, School of Materials Science and Engineering, Nanjing University of Science and Technology, Nanjing 210094, China
 - ² Australian Institute for Bioengineering and Nanotechnology, The University of Queensland, Brisbane 4072, Australia
 - ³ X-ray Sciences Division, Argonne National Laboratory, Lemont, IL 60439, USA
 - ⁴ College of Mechatronics and Control Engineering, Shenzhen University, Shenzhen 518060, China
 - ⁵ Suzhou Nuclear Powder Research Institute Co., Ltd., Suzhou 215004, China
 - ⁶ Institute for Nanotechnology, Karlsruhe Institute of Technology, 76344 Eggenstein-Leopoldshafen, Germany
 - ⁷ Department of Physics, City University of Hong Kong, Kowloon 999077, Hong Kong SAR, China
 - ⁸ Center for Neutron Scattering and Applied Physics, City University of Hong Kong Dongguan Research Institute, Dongguan 523000, China
 - ⁹ Shenzhen Research Institute, City University of Hong Kong, Shenzhen 518057, China
- * Correspondence: hezhu@njust.edu.cn (H.Z.); lansi@njust.edu.cn (S.L.)
† These authors contributed equally to this work.



Citation: Qin, Y.; Zhang, W.; Li, K.; Fu, S.; Lou, Y.; Liu, S.; Ge, J.; Ying, H.; Liu, W.-D.; Zuo, X.; et al. Engineering Atomic-to-Nano Scale Structural Homogeneity towards High Corrosion Resistance of Amorphous Magnesium-Based Alloys. *Micromachines* **2022**, *13*, 1992. <https://doi.org/10.3390/mi13111992>

Academic Editor: Chang-Hwan Choi

Received: 19 October 2022

Accepted: 15 November 2022

Published: 17 November 2022

Publisher's Note: MDPI stays neutral with regard to jurisdictional claims in published maps and institutional affiliations.



Copyright: © 2022 by the authors. Licensee MDPI, Basel, Switzerland. This article is an open access article distributed under the terms and conditions of the Creative Commons Attribution (CC BY) license (<https://creativecommons.org/licenses/by/4.0/>).

Abstract: Magnesium-based amorphous alloys have aroused broad interest in being applied in marine use due to their merits of lightweight and high strength. Yet, the poor corrosion resistance to chloride-containing seawater has hindered their practical applications. Herein, we propose a new strategy to improve the chloride corrosion resistance of amorphous Mg₆₅Cu₁₅Ag₁₀Gd₁₀ alloys by engineering atomic-to-nano scale structural homogeneity, which is implemented by heating the material to the critical temperature of the liquid–liquid transition. By using various electrochemical, microscopic, and spectroscopic characterization methods, we reveal that the liquid–liquid transition can rearrange the local structural units in the amorphous structure, slightly decreasing the alloy structure's homogeneity, accelerate the formation of protective passivation film, and, therefore, increase the corrosion resistance. Our study has demonstrated the strong coupling between an amorphous structure and corrosion behavior, which is available for optimizing corrosion-resistant alloys.

Keywords: magnesium-based alloy; liquid–liquid phase transition; corrosion resistance; structural homogeneity

1. Introduction

Magnesium (Mg) alloys are considered one of the most promising lightweight metals to potentially replace heavier structural materials in the uses of aerospace, marine, and automobile vehicles [1,2]. However, despite the great prospect, Mg alloys still suffer from a number of inherent drawbacks, including the strength–corrosion tradeoff [3,4]. In this regard, many efforts have been devoted to employing amorphous Mg alloys for anti-corrosion uses. Here, an amorphous alloy means that all the metallic atoms in the long range are arranged randomly in the structure. It is found that amorphous magnesium-based alloys are attractive for their high mechanical properties [5,6]. In addition, amorphous alloys also exhibit improved corrosion resistance due to the chemical homogeneity with reduced crystallographic breaks such as grain boundaries, dislocations, and phase segregations, so

the chemical attack on those susceptible sites can be largely avoided [7,8]. Nevertheless, for the Mg-based amorphous alloys in particular, the high reactivity of Mg still makes the material vulnerable to corrosion failure [9,10]. To further improve the corrosion resistance of the Mg-based amorphous alloys, previous efforts mainly focus on strategies of surface modifications [11,12] and on alloying corrosion-resistant elements like Nb [13]. Furthermore, forming a passivation film on the alloy surface is also an effective way to prevent corrosion [14,15]. Although various progress has been achieved, the critical barrier has not yet been overcome, which severely hinders the widespread usage of Mg-based amorphous alloys [16,17]. Therefore, more rational and artful ideas for material design down to the nanostructural or atomic level are highly desired for improving the corrosion resistance of the amorphous Mg alloys.

When heating amorphous alloys before melting, typically, several phase transition processes occur in sequence, including separation into amorphous phases with different components [18,19], liquid–liquid phase transition [20,21], and crystallization [22,23]. Among these processes, the liquid–liquid phase transition involves only rearrangement of local structural units and no component variation in the amorphous alloys without a long-range order [24,25]. Although local changes in structure and density are subtle and come with a small amount of heat release, it still makes remarkable differences in mechanical and functional properties [26,27]. Studies show that the liquid–liquid transition is closely related to the thermodynamic stability and mechanical properties of Mg-based amorphous alloys [28]. The thermodynamically-favored local order and loose structure emerge during the liquid–liquid transition, which benefits higher hardness and modulus than a completely disordered structure. In addition, Hu et al. [29] reveal that the metastable state formed during the liquid–liquid transition in $(\text{Fe}_{0.72}\text{B}_{0.24}\text{Nb}_{0.04})_{95.5}\text{Y}_{4.5}$ amorphous ribbon could significantly reduce the activation energy and reaction energy barrier of high-temperature oxidization. More importantly, by using synchrotron small-angle scattering, our group has demonstrated that the liquid–liquid phase transition can significantly impact the atomic-to-nano scale homogeneity in the medium-range structure of amorphous Mg alloys [28], which is strongly related to the corrosion resistance of the material [30–33]. This motivates us to fundamentally understand the correlation between liquid–liquid transition and corrosion, improving the corrosion resistance in amorphous Mg-based alloys.

In this work, by selecting $\text{Mg}_{65}\text{Cu}_{15}\text{Ag}_{10}\text{Gd}_{10}$ amorphous alloy as a model material, we reveal that the chloride corrosion resistance of Mg-based alloys could be significantly improved by rearranging the local structural unit in the liquid–liquid transition. By means of potentiodynamic polarization measurement, electrochemical impedance test, immersion test, differential scanning calorimetry, high energy X-ray diffractometry, high-resolution transmission electron microscopy, X-ray photoelectron spectroscopy, and scanning electron microscopy, it is revealed that structural ordering and heterogeneity during the liquid–liquid transition accelerate the formation of the passivation film and therefore improve the corrosion resistance of the Mg-based alloy. This study proves the strong correlation between an amorphous structure and corrosion behavior and provides a new strategy for optimizing corrosion-resistance alloys.

2. Experimental Method

2.1. Sample Preparation

The target material studied in this paper was $\text{Mg}_{65}\text{Cu}_{15}\text{Ag}_{10}\text{Gd}_{10}$ amorphous alloy (by atomic percentage), with the purity of raw materials being 99.95 wt.%. In order to ensure uniform mixing of each component, the total metal mass was controlled for no more than 10 g. The surface oxide of raw materials was removed by file and sandpaper, and the mass error of weighing did not exceed 0.001 g.

The alloy ingot was prepared by induction heating and then vacuum arc melting many times. The chamber vacuum was below 1×10^{-3} Pa and then filled with high-purity argon gas at -0.5 Pa as protection. Then, the quartz tube containing the alloy ingot was placed inside a copper induction coil and electrified by a current of 50 A. Due to the pressure

difference, the molten alloy ingot was ejected through a 0.9 mm hole onto the rotating copper roller at a high speed of 60 rps. Eventually, the amorphous ribbons were obtained. A few of them were heated to the temperature of liquid–liquid transition (i.e., T_C) (444 K) in the oven, hereafter referred to as the T_C -treated samples. The T_C is determined by the temperature at an abnormal exothermic peak in differential scanning calorimetry (DSC), which will be discussed later.

2.2. Corrosion Resistance Test

Prior to the corrosion experiments, both as-cast and heated ribbon specimens were cut to 10 mm \times 2 mm, fixed in epoxy resin, polished with 2000 mesh sandpaper, and then sonicated in acetone, ethanol, and deionized water, respectively. The electrochemical experiments were carried out using the CHI660E A20146 electrochemistry workstation. The reference electrode and counter electrode were saturated calomel electrode (SCE) and Pt, respectively. The potential polarization scanning was started at 150 mV below the open circuit potential (OCP) at a rate of 0.833 V \cdot s $^{-1}$ in both 1 mol \cdot L $^{-1}$ NaCl and 1 mol \cdot L $^{-1}$ NaOH solutions. Electrochemical impedance spectroscopy (EIS) was performed at the frequency ranging from 10 5 to 10 $^{-2}$ Hz with an amplitude of 5 mV. The solutions of the immersion test lasting 2 h were 0.01 mol \cdot L $^{-1}$ NaCl and 0.01 mol \cdot L $^{-1}$ NaOH.

2.3. Characterization Techniques

A total of 20 mg Mg $_{65}$ Cu $_{15}$ Ag $_{10}$ Gd $_{10}$ ribbon was used to test the thermophysical parameters by differential scanning calorimetry (DSC, METTLER TOLEDO) at a heating rate of 10 K \cdot min $^{-1}$. The nitrogen flow rate was set to 50 mL \cdot min $^{-1}$ to isolate oxygen and prevent drastic oxidation of the sample during the heating process. High-resolution transmission electron microscopy (HRTEM, FEI TECNAL G2 20), small-angle synchrotron X-ray scattering (SAXS, Advanced Photon Source of Argonne National Laboratory), and high energy X-ray diffractometry (HEXRD) were used to probe the alloy microstructure. The thin region of the HRTEM sample was obtained by etching the amorphous ribbon with an incident angle of 8 $^\circ$ and an energy of 8 keV at low temperature of liquid nitrogen for 25 min. The beam size of the synchrotron X-ray ($\lambda = 0.0886$ nm) was 0.1 \times 0.2 mm and the SAXS data with Q range from 0.0034 to 0.364. \AA^{-1} was calibrated and corrected by empty cell scattering, transmission, and detector response using a beamline MATLAB program package [34]. The incident wavelength of the HEXRD excited by Ag K α 1 was 0.05594 nm (22 keV), and the scattering angle (2θ) ranged from 5 $^\circ$ to 20 $^\circ$. The surface morphology of the samples was characterized by scanning electron microscopy (SEM, JSM-IT500HR) with an electron beam voltage of 20 kV. The surface composition and valence state of the alloy were analyzed by X-ray photoelectron spectroscopy (XPS, Thermo Fisher Scientific K-Alpha) with monochromatic Al K α ray ($h\nu = 1486.6$ eV) radiation.

3. Results and Discussion

3.1. Microstructure and Thermal Analysis

The differential scanning calorimetry (DSC) curve of Mg $_{65}$ Cu $_{15}$ Ag $_{10}$ Gd $_{10}$ amorphous alloys (Figure 1a) shows an abnormal exothermic peak that appeared after the glass transition temperature T_g (422 K) [35]. The corresponding temperature was marked as T_C (444 K), which, according to previous studies, is related to the liquid–liquid phase transition [28,36]. As the temperature continues to increase, a sharp exothermic peak starting at 458 K emerges, which can be assigned to the crystallization of the amorphous material [37]. The width and thickness of the ribbons are 2 mm and 45 μ m, respectively (Figure 1a inset).

From the HRTEM image of the T_C -treated sample (Figure 1b), the atoms are arranged in a maze-like disordered manner, whereas the selected area electron diffraction (SAED) pattern in the inset shows broad and dispersive rings. The results further demonstrate that the Mg $_{65}$ Cu $_{15}$ Ag $_{10}$ Gd $_{10}$ alloys remain the amorphous feature after T_C treatment.

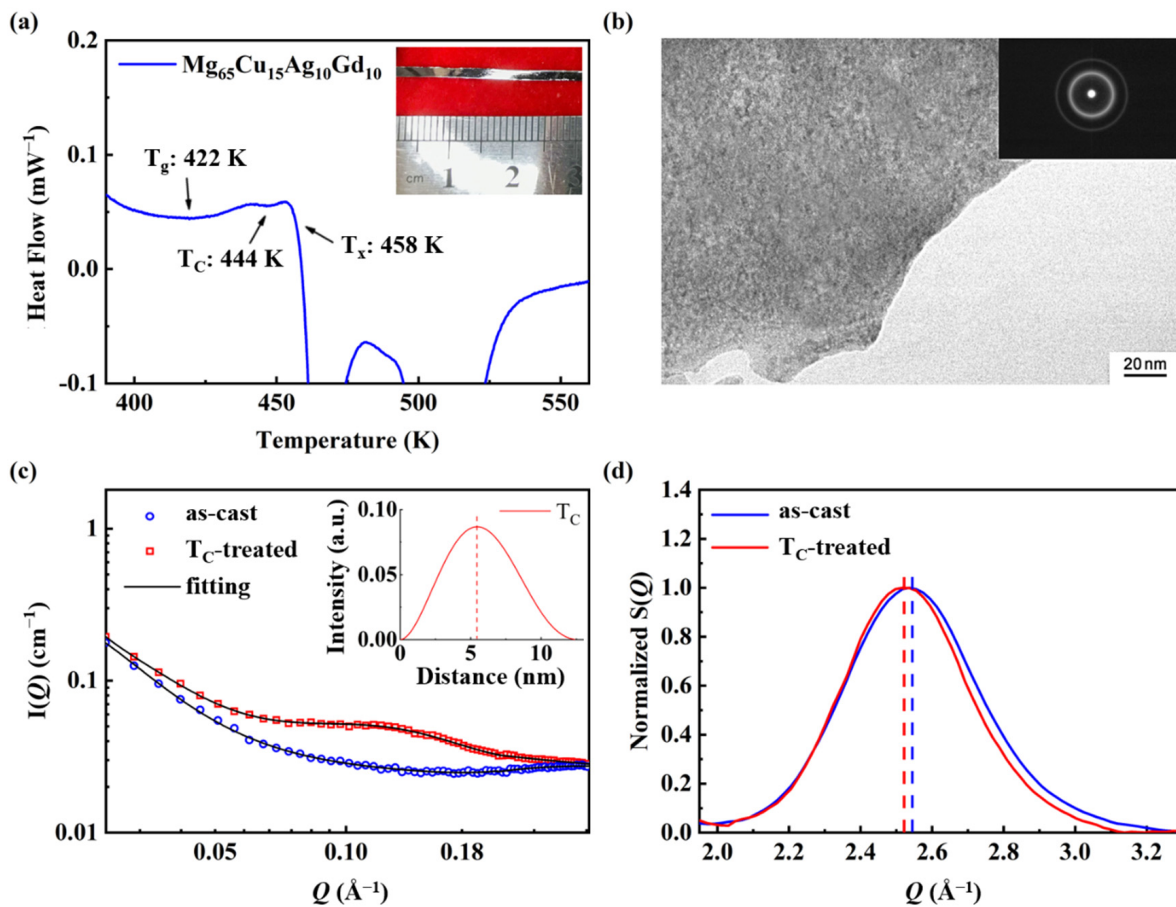


Figure 1. (a) Differential scanning calorimetry curve of $\text{Mg}_{65}\text{Cu}_{15}\text{Ag}_{10}\text{Gd}_{10}$ amorphous alloy ribbon. The inset is an optical image of an as-cast sample. (b) High-resolution transmission electron microscopy of $\text{Mg}_{65}\text{Cu}_{15}\text{Ag}_{10}\text{Gd}_{10}$ T_C -treated ribbon. The inset is the selected area electron diffraction pattern. (c) The SAXS of $\text{Mg}_{65}\text{Cu}_{15}\text{Ag}_{10}\text{Gd}_{10}$ as-cast and T_C -treated ribbons. Reproduced with permission [28]. Copyright 2021, Springer Nature. The inset is the size distribution function based on the SAXS profiles. (d) The structure factor of $\text{Mg}_{65}\text{Cu}_{15}\text{Ag}_{10}\text{Gd}_{10}$ as-cast and T_C -treated ribbons.

Down to the nanoscale, an interference peak occurs in the T_C -treated sample whereas it does not exist in the as-cast sample according to the results of SAXS (Figure 1c), which suggests the occurrence of nanoscale heterogeneity different from the amorphous matrix in the T_C -treated sample [28,38–40]. Furthermore, a spheroid model with polydispersity is employed to fit the SAXS profile of the T_C -treated sample, and the obtained size distribution function result is displayed in Figure 1c inset [41,42]. It is seen that the diameter of the spheroidal granular-like structure is around 5.4 nm for the T_C -treated sample, verifying that the heterogeneous structure exists [43–45]. Further down to the atomic scale, Figure 1d compares the structure factor ($S(Q)$) patterns as a function of momentum transfer amplitude (Q) for both the as-cast and T_C -treated alloys. The first $S(Q)$ peak shows a lower peak position and a narrower peak width after T_C treatment, which indicates that the local order is extended to the medium range and the atomic packing is less dense than the matrix. The structural correlation is enhanced from the short to the medium range (~ 5 – 10 Å) during this process, due to the recombination of the local atomic units [22,46,47]. To summarize, the nanoscale thermodynamically-favored metastable amorphous heterogeneous region with an average diameter of 5.4 nm is uniformly distributed in the amorphous alloy matrix. In each heterogeneous region, the degree of the atomic order is extended to the medium range (~ 5 – 10 Å). The heterogeneity in the atomic-to-nano scale stands for the liquid–liquid transition and the strong connection between abnormal exothermic peak at T_C and liquid–liquid transition is consistent with our previous studies [28,48,49].

3.2. Analysis of Potentiodynamic Corrosion Behavior

Figure 2a shows the potentiodynamic polarization curves of the $Mg_{65}Cu_{15}Ag_{10}Gd_{10}$ as-cast and T_C -treated samples in $1 \text{ mol}\cdot\text{L}^{-1}$ NaCl solution, showing an active dissolution process through anodic polarization. By using the Tafel extrapolation method, the self-corrosion potential of the as-cast and T_C -treated samples were -1.14 V and -1.11 V , respectively, and the corresponding self-corrosion current densities were $1.1 \times 10^{-3} \text{ A}\cdot\text{cm}^{-2}$ and $5.3 \times 10^{-4} \text{ A}\cdot\text{cm}^{-2}$, respectively. The higher corrosion potential and lower corrosion current of the T_C -treated sample indicate that the chemical stability in the NaCl solution is enhanced after the T_C heat treatment. Figure 2a inset shows the curve of open circuit potential of the as-cast and T_C -treated samples as a function of immersion time in $1 \text{ mol}\cdot\text{L}^{-1}$ NaCl electrolyte. In the first 100 s, the OCP of the amorphous ribbons changes rapidly to positive, indicating that their stability increases due to the construction of the surface film. Subsequently, the OCP curves of these two samples gradually become stable, with a slight fluctuation in a certain potential, which is attributed to the loss and regrowth of the passivation layer on the surface. During the last 300 s immersion, the OCP of the T_C -treated sample is higher than that of the as-cast sample, indicating that a better defense and stability layer is formed on the surface of the T_C -treated sample.

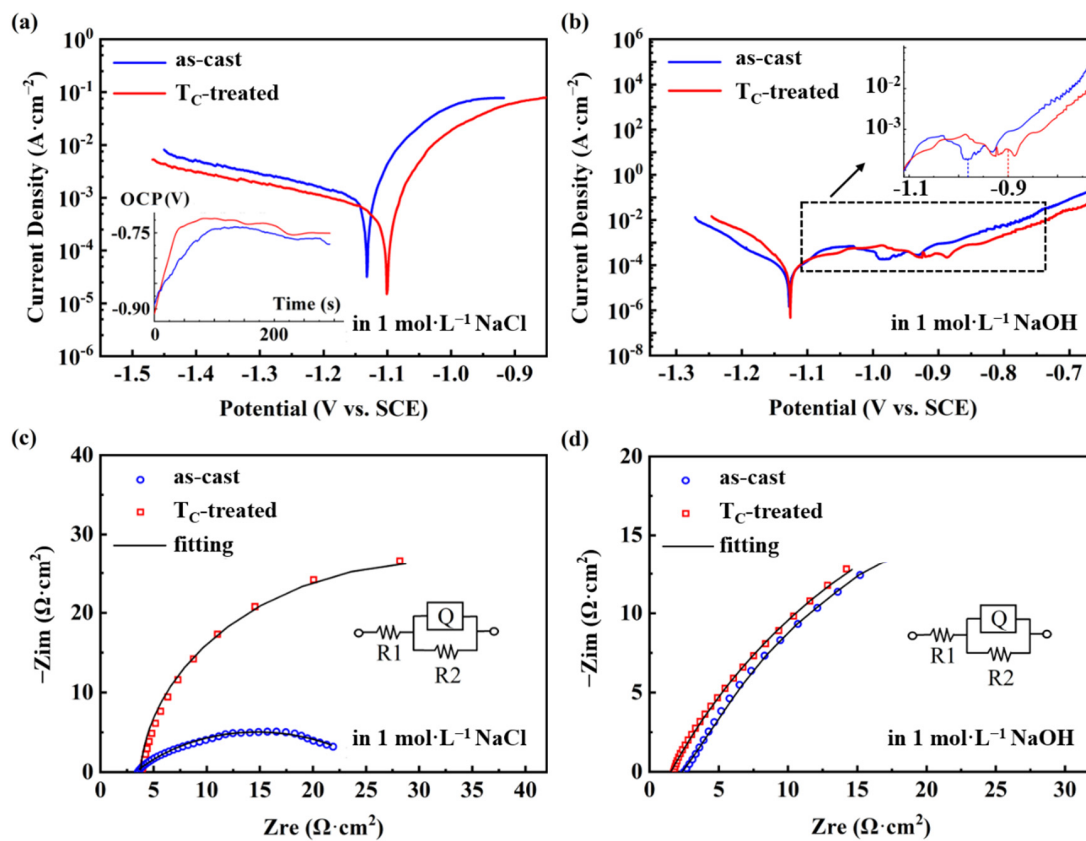


Figure 2. (a) Potentiodynamic polarization curves of as-cast and T_C -treated samples in 1 M NaCl solution. The inset is their open circuit potential (V vs. SCE) curves dependent on the immersion time. (b) Potentiodynamic polarization curves of as-cast and T_C -treated samples in 1 M NaOH solution. The inset enlarges the breakdown potential with the same coordinate units. (c) Nyquist curves of as-cast and T_C -treated samples in 1 M NaCl solution. (d) Nyquist curves of as-cast and T_C -treated samples in 1 M NaOH solution.

Figure 2b shows the potentiodynamic polarization curves of the as-cast and T_C -treated $Mg_{65}Cu_{15}Ag_{10}Gd_{10}$ samples in $1 \text{ mol}\cdot\text{L}^{-1}$ NaOH solution, both of which exhibit good chemical stability with a corrosion current of about $1 \times 10^{-5} \text{ A}\cdot\text{cm}^{-2}$ and a corrosion potential of -1.13 V . A spontaneous passivation occurs for both of the materials with a low passivation

current density of about $3 \times 10^{-4} \text{ A}\cdot\text{cm}^{-2}$. Although both the materials show a wide passivation zone ($-1.10 \sim -0.98 \text{ V}$ for the as-cast sample vs. $-1.10 \sim -0.90 \text{ V}$ for the T_C -treated sample), the passivation film breakdown potential of the T_C -treated sample is slightly higher, indicating that the passivation film of the T_C -treated sample is more stable [50]. When applying the potential to above -0.90 V , the passivation films of these two samples are transpassively dissolved, and accordingly, the corrosion current density increases [51]. All the above results indicate that the $\text{Mg}_{65}\text{Cu}_{15}\text{Ag}_{10}\text{Gd}_{10}$ amorphous alloy system shows better corrosion resistance after T_C treatment in both NaCl and NaOH solutions.

Figure 2c,d show the EIS fitting circuits in $1 \text{ mol}\cdot\text{L}^{-1}$ NaCl and $1 \text{ mol}\cdot\text{L}^{-1}$ NaOH solutions, respectively. The fitted circuit elements include solution resistance (R1), charge transfer resistance (R2), and constant phase element (Q), and the fitted results are shown in Table 1. After T_C treatment, the corrosion behavior does not change compared with the as-cast one, and all the EIS curves in NaCl and NaOH solutions show a single capacitive arc with one time constant [52]. From the fitting results, the R2 values of the T_C -treated samples are higher than those of the as-cast samples in both NaCl and NaOH solutions. The larger R2 is inclined towards a higher corrosion potential, lower corrosion current, and higher passivation film breakdown potential, which is consistent with the potentiodynamic polarization results (Figure 2a,b) [53].

Table 1. EIS fitting parameters of as-cast and T_C -treated samples of all the same size in 1 M NaCl and NaOH solutions.

	Q ($\mu\text{s}^0/\Omega$)	α	R1 ($\Omega\cdot\text{cm}^2$)	R2 ($\Omega\cdot\text{cm}^2$)
as-cast in 1 M NaCl	421.1	0.56	2.77	24.00
T_C -treated in 1 M NaCl	1000.0	1.00	3.70	56.06
as-cast in 1 M NaOH	545.1	0.65	2.51	81.72
T_C -treated in 1 M NaOH	77.99	0.77	2.45	84.24

3.3. Analysis of Immersion Corrosion Behavior

Figure 3 shows the SEM images of the as-cast and T_C -treated $\text{Mg}_{65}\text{Cu}_{15}\text{Ag}_{10}\text{Gd}_{10}$ metal glass ribbons soaked in $0.01 \text{ mol}\cdot\text{L}^{-1}$ NaCl and $0.01 \text{ mol}\cdot\text{L}^{-1}$ NaOH solutions for 2 h. The passivation films of the as-cast ribbon in $0.01 \text{ mol}\cdot\text{L}^{-1}$ NaCl show local corrosion and cracks (arrows in Figure 3a), which are largely inhibited in the T_C -treated sample (Figure 3b). The higher corrosion resistance of the T_C -treated sample also verifies the experimental results of potentiodynamic polarization curves and EIS. Analogously, the corrosion resistance of the T_C -treated $\text{Mg}_{65}\text{Cu}_{15}\text{Ag}_{10}\text{Gd}_{10}$ ribbon in $0.01 \text{ mol}\cdot\text{L}^{-1}$ NaOH solution is a little better than that of the as-cast sample, which is inferred by the disappearing pits after the T_C treatment.

In order to better understand the chemical stability of the $\text{Mg}_{65}\text{Cu}_{15}\text{Ag}_{10}\text{Gd}_{10}$ amorphous alloys, XPS measurements were performed on the as-cast and T_C -treated ribbons immersed in 0.01 M NaCl and 0.01 M NaOH for 2 h (Figure 4a,b). The relevant elemental content obtained from XPS is displayed in Table 2. For the as-cast samples, the Ag content is lower than the designed composition, which is related to the highest antioxidative activities of Ag [54]. Remarkably, the Mg content is much higher than the designed ratio, indicating the passivation film on the surface of the ribbon is dominated by MgO. When subjected to the T_C treatment, the Mg content on the surface of the T_C -treated sample relative to the as-cast sample decreases remarkably in NaCl. This phenomenon firmly validates the improved corrosion to NaCl for the T_C -treated alloy. For the samples in NaOH, the Mg content of the T_C -treated sample is similar to that of the as-cast sample. This is because of the higher corrosion resistance of the prepared alloy in NaOH. Chloride ions are highly corrosive because they, with a small radius and strong permeability, could penetrate the relatively loose passivation film into the matrix and act as ionic conductors to accelerate the anodic polarization corrosion of alloy [55]. Figure 4c,d show the corresponding high-resolution Mg 1s spectra. The peak located at 1303.57 eV corresponds to Mg metal [56], whereas the peak at 1304.36 eV can be assigned to Mg^{2+} [57]. A lower Mg^{2+} content is detected in the T_C -treated sample by comparing the XPS spectra of NaCl-soaked ribbons, indicating that the T_C heat treatment could effectively protect Mg from oxidation corrosion.

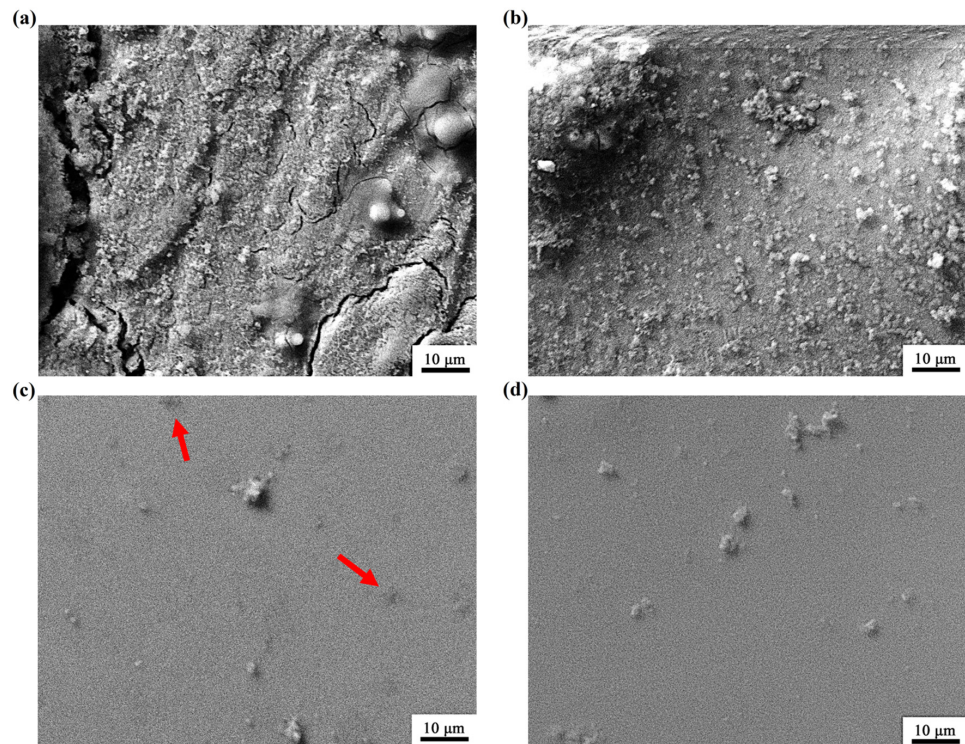


Figure 3. SEM images of (a) as-cast and (b) T_C -treated samples after a 2-h immersion in 0.01 M NaCl solution. SEM images of (c) as-cast and (d) T_C -treated samples after a 2-h immersion in 0.01 M NaOH solution. The red arrows in Figure 3c show the corrosion pits induced by the NaOH solution.

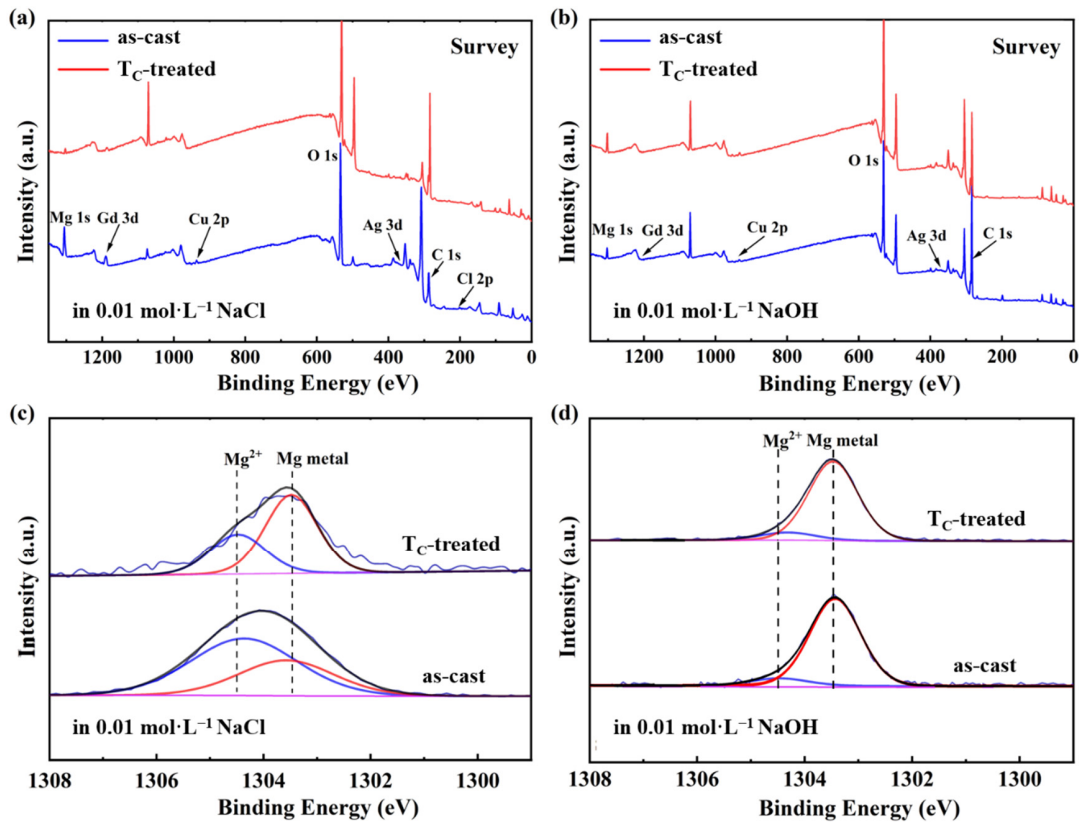


Figure 4. (a) Surface XPS of as-cast and T_C -treated samples after a 2-h immersion in 0.01 M NaCl solution. (b) Surface XPS of as-cast and T_C -treated samples after a 2-h immersion in 0.01 M NaOH solution. (c) Mg 1s spectra of as-cast and T_C -treated samples after a 2-h immersion in 0.01 M NaCl solution. (d) Mg 1s spectra of as-cast and T_C -treated samples after a 2-h immersion in 0.01 M NaOH solution.

Table 2. Atomic ratios of elements on the surfaces of as-cast and T_C -treated samples after a 2-h immersion in 0.01 M NaCl and NaOH solutions.

	Mg	Cu	Ag	Gd	O	Cl	Total
as-cast in 0.01 M NaCl	13.49	1.32	0.25	0.31	83.02	1.61	100
T_C -treated in 0.01 M NaCl	3.49	0.66	0.33	0.18	93.77	1.57	100
as-cast in 0.01 M NaOH	8.04	1.54	0.56	0.31	89.55	-	100
T_C -treated in 0.01 M NaOH	11.07	1.14	0.43	0.16	87.20	-	100

3.4. Discussion

Replacing Cu in the traditional ternary $Mg_{65}Cu_{25}Gd_{10}$ amorphous alloy with Ag element to form a quaternary $Mg_{65}Cu_{15}Ag_{10}Gd_{10}$ one was an excellent way to improve corrosion resistance because of the higher equilibrium electrode potential of Ag, namely better chemical stability, than that of Cu [58]. Our experimental results of electrochemical and microscopic tests, as well as XPS, confirm the excellent alkali corrosion resistance of the amorphous $Mg_{65}Cu_{15}Ag_{10}Gd_{10}$ alloy system.

The improvement in chemical stability, i.e., corrosion performance, could be related to the thermodynamically-favored change in microstructure brought by the liquid–liquid transition. During the liquid–liquid phase transition, a medium-range ordered structure shows higher thermodynamic stability than the totally disordered structure. So, spontaneously, combinations of local atomic units occur, forming nanoscale “medium-range-ordered island” distributed heterogeneously within the amorphous matrix [59–61]. Driven by this structural change, the electrochemical reaction of micro galvanic cells formed by the fluctuation of surface energy is small in area and large in quantity, so the formation of passivation film is accelerated. In this micro galvanic cell, the alloy matrix acts as a cathode, whereas the amorphous heterogeneous structure acts as an anode. The area of the cathode matrix is much larger than that of the active amorphous heterogeneous structure anode, which ensures the electrochemical reaction of the passivation film generation at the early stage of corrosion. To sum up the above, the corrosion is accelerated at the beginning of the corrosion process in the T_C -treated sample. As a result, at the beginning of the corrosion, the T_C -treated sample could evenly form more corrosion products quickly. When the formation rate of the passivation film is higher than the dissolution rate, compact and uniform passivation film would be formed to prevent the solution from entering the matrix and causing further corrosion, meaning that the alloy possesses good chemical stability. The higher R_2 value of the EIS results of the T_C -treated sample clearly demonstrates that the passivation film of the T_C -treated sample is not prone to be dissolved. Note that the liquid–liquid transition does not result in structural incoherence, such as grain boundary and dislocation, so the T_C -treated sample is less likely to corrode by a network [62].

4. Conclusions

This paper reports a new approach to improve the corrosion resistance of a typical Mg-based amorphous alloy $Mg_{65}Cu_{15}Ag_{10}Gd_{10}$ of an anomalous exothermic peak by heating the material to the T_C temperature of liquid–liquid transition. During this transition, the structural homogeneity slightly decreases with the rearrangement of the local structural units, which accelerates the formation of protective passivation film and therefore increases the corrosion resistance of the Mg-based alloy. Our present study has initiated a new route to optimize corrosion resistance by engineering atomic-to-nano scale structural homogeneity, which could be applied to other amorphous alloy systems with the liquid–liquid phase transition and hopefully extended to widespread corrosion-resistant alloy research.

Author Contributions: Conceptualization, S.L. (Si Lan), H.H. and X.-L.W.; methodology, K.L. and S.F.; software, Y.L., S.L. (Sinan Liu) and H.Y.; formal analysis, Y.Q., W.Z. and J.G.; investigation, Y.Q., W.Z. and J.G.; data curation, X.Z. and Y.R.; writing—original draft preparation, Y.Q. and H.Z.; writing—review and editing, H.Z. and S.L. (Si Lan); visualization, W.-D.L. and Z.W.; supervision,

H.Z. and S.L. (Si Lan); funding acquisition, J.S., S.-C.W. and S.L. (Si Lan); All authors have read and agreed to the published version of the manuscript.

Funding: This work was financially supported by the National Key R&D Program of China No. 2021YFB3802800, the National Natural Science Foundation of China (Grant Nos. 52222104, 51871120, 22275089), the Natural Science Foundation of Jiangsu Province (Grant No. BK20200019), the Shenzhen Science and Technology Innovation Commission (No. JCYJ20200109105618137), the Fundamental Research Funds for the Central Universities (No. 30922010307), and the support by Guangdong-Hong Kong-Macao Joint Laboratory for Neutron Scattering Science. The synchrotron diffraction and small-angle X-ray scattering experiments were carried out at the Advanced Photon Source, a US Department of Energy (DOE) Office of Science User Facility operated for the DOE Office of Science by Argonne National Laboratory under Contract No. DE-AC02-06CH11357.

Data Availability Statement: The data that support the findings of this study are available from the authors upon reasonable request.

Conflicts of Interest: The authors declare no conflict of interest.

References

1. Bhattacharjee, T.; Suh, B.C.; Sasaki, T.T.; Ohkubo, T.; Kim, N.J.; Hono, K. High strength and formable Mg–6.2Zn–0.5Zr–0.2Ca alloy sheet processed by twin roll casting. *Mater. Sci. Eng. A* **2014**, *609*, 154–160. [[CrossRef](#)]
2. Zeng, Z.; Nie, J.F.; Xu, S.W.; HJ Davies, C.; Birbilis, N. Super-formable pure magnesium at room temperature. *Nat. Commun.* **2017**, *8*, 972. [[CrossRef](#)] [[PubMed](#)]
3. Wang, Y.; Liu, B.; Zhao, X.A.; Zhang, X.; Miao, Y.; Yang, N.; Yang, B.; Zhang, L.; Kuang, W.; Li, J.; et al. Turning a native or corroded Mg alloy surface into an anti-corrosion coating in excited CO₂. *Nat. Commun.* **2018**, *9*, 4058. [[CrossRef](#)] [[PubMed](#)]
4. Zhao, M.C.; Liu, M.; Song, G.; Atrens, A. Influence of the β -phase morphology on the corrosion of the Mg alloy AZ91. *Corros. Sci.* **2008**, *50*, 1939–1953. [[CrossRef](#)]
5. Inoue, A.; Ohtera, K.; Kita, K.; Masumoto, T. New Amorphous Mg–Ce–Ni Alloys with High Strength and Good Ductility. *Jpn. J. Appl. Phys.* **1988**, *27*, L2248. [[CrossRef](#)]
6. Gonzalez, S.; Figueroa, I.A.; Todd, I. Influence of minor alloying additions on the glass-forming ability of Mg–Ni–La bulk metallic glasses. *J. Alloys Compd.* **2009**, *484*, 612–618. [[CrossRef](#)]
7. Wang, C.; Shuai, Y.; Yang, Y.; Zeng, D.; Liang, X.; Peng, S.; Shuai, C. Amorphous magnesium alloy with high corrosion resistance fabricated by laser powder bed fusion. *J. Alloys Compd.* **2022**, *897*, 163247. [[CrossRef](#)]
8. Wang, J.; Huang, S.; Wei, Y.; Guo, S.; Fusheng, P. Enhanced mechanical properties and corrosion resistance of a Mg–Zn–Ca bulk metallic glass composite by Fe particle addition. *Mater. Lett.* **2013**, *91*, 311–314. [[CrossRef](#)]
9. Romzi, M.A.F.; Alias, J.; Ramli, M.I.M. Effect of zinc (Zn) on the microstructure and corrosion behaviour of magnesium (Mg). *Mater. Today Proc.* **2022**, *48*, 1873–1879. [[CrossRef](#)]
10. Matias, T.B.; Roche, V.; Nogueira, R.P.; Asato, G.H.; Kiminami, C.S.; Bolfarini, C.; Botta, W.J.; Jorge, A.M., Jr. Mg–Zn–Ca amorphous alloys for application as temporary implant: Effect of Zn content on the mechanical and corrosion properties. *Mater. Des.* **2016**, *110*, 188–195. [[CrossRef](#)]
11. Chen, S.; Tu, J.; Hu, Q.; Xiong, X.; Wu, J.; Zou, J.; Zeng, X. Corrosion resistance and in vitro bioactivity of Si-containing coating prepared on a biodegradable Mg–Zn–Ca bulk metallic glass by micro-arc oxidation. *J. Non-Cryst. Solids* **2017**, *456*, 125–131. [[CrossRef](#)]
12. Zai, W.; Sun, S.; Man, H.C.; Lian, J.; Zhang, Y. Preparation and anticorrosion properties of electrodeposited calcium phosphate (CaP) coatings on Mg–Zn–Ca metallic glass. *Mater. Chem. Phys.* **2022**, *290*, 126532. [[CrossRef](#)]
13. Guan, W.; Cui-Xia, G.; Shu-Jie, P. Thermal stability, mechanical properties and corrosion behavior of a Mg–Cu–Ag–Gd metallic glass with Nb addition. *Rare Met.* **2017**, *36*, 183–187.
14. Guoqiang, L.; Lijing, Z.; Huanxi, L. Corrosion behavior of the bulk amorphous Mg₆₅Cu₂₅Gd₁₀ alloy. *Rare Met. Mater. Eng.* **2009**, *38*, 110–114.
15. Sun, Y.; Li, Z.; Liu, J.; Liang, Z. Corrosion characteristics of Mg–Cu–Gd amorphous alloys. *J. Nanjing Univ. Aeronaut. Astronaut.* **2010**, *42*, 636–640.
16. Zai, W.; Man, H.C.; Su, Y.; Li, G.; Lian, J. Impact of microalloying element Ga on the glass-forming ability (GFA), mechanical properties and corrosion behavior of Mg–Zn–Ca bulk metallic glass. *Mater. Chem. Phys.* **2020**, *255*, 123555. [[CrossRef](#)]
17. Li, H.; Pang, S.; Liu, Y.; Sun, L.; Liaw, P.K.; Zhang, T. Biodegradable Mg–Zn–Ca–Sr bulk metallic glasses with enhanced corrosion performance for biomedical applications. *Mater. Des.* **2015**, *67*, 9–19. [[CrossRef](#)]
18. Park, E.S.; Jeong, E.Y.; Lee, J.K.; Bae, J.C.; Kwon, A.R.; Gebert, A.; Schultz, L.; Chang, H.J.; Kim, D.H. In situ formation of two glassy phases in the Nd–Zr–Al–Co alloy system. *Scr. Mater.* **2007**, *56*, 197–200. [[CrossRef](#)]
19. Sarlar, K.; Kucuk, I. Phase separation and glass forming ability of (Fe_{0.72}Mo_{0.04}B_{0.24})(100–x)Gd–x (x = 4, 8) bulk metallic glasses. *J. Non-Cryst. Solids* **2016**, *447*, 198–201. [[CrossRef](#)]

20. Lan, S.; Ren, Y.; Wei, X.Y.; Wang, B.; Gilbert, E.P.; Shibayama, T.; Watanabe, S.; Ohnuma, M.; Wang, X.L. Hidden amorphous phase and reentrant supercooled liquid in Pd-Ni-P metallic glasses. *Nat. Commun.* **2017**, *8*, 14679. [[CrossRef](#)]
21. Ge, J.; He, H.; Zhou, J.; Lu, C.; Dong, W.; Liu, S.; Lan, S.; Wu, Z.; Wang, A.; Wang, L.; et al. In-situ scattering study of a liquid-liquid phase transition in Fe-B-Nb-Y supercooled liquids and its correlation with glass-forming ability. *J. Alloys Compd.* **2019**, *787*, 831–839. [[CrossRef](#)]
22. Liu, S.; Ge, J.; Ying, H.; Lu, C.; Ma, D.; Wang, X.L.; Zuo, X.; Ren, Y.; Feng, T.; Shen, J.; et al. In Situ Scattering Studies of Crystallization Kinetics in a Phase-Separated Zr-Cu-Fe-Al Bulk Metallic Glass. *Acta Metall. Sin. Engl. Lett.* **2022**, *35*, 103–114. [[CrossRef](#)]
23. Lan, S.; Wei, X.; Zhou, J.; Lu, Z.; Wu, X.; Feygenson, M.; Neufeind, J.; Wang, X.L. In-situ study of crystallization kinetics in ternary bulk metallic glass alloys with different glass forming abilities. *Appl. Phys. Lett.* **2014**, *105*, 201906. [[CrossRef](#)]
24. Lan, S.; Dong, W.X.; Wang, X.L. The progress of research on anomalous exothermic phenomenon and hidden amorphous phase transition in metallic glasses. *Chin. J. Nat.* **2017**, *39*, 327–339.
25. Sheng, H.W.; Liu, H.Z.; Cheng, Y.Q.; Wen, J.; Lee, P.L.; Luo, W.K.; Shastri, S.D.; Ma, E. Polyamorphism in a metallic glass. *Nat. Mater.* **2007**, *6*, 192–197. [[CrossRef](#)] [[PubMed](#)]
26. Liu, S.; Wang, L.; Ge, J.; Wu, Z.; Ke, Y.; Li, Q.; Sun, B.; Feng, T.; Wu, Y.; Wang, J.T.; et al. Deformation-enhanced hierarchical multiscale structure heterogeneity in a Pd-Si bulk metallic glass. *Acta Mater.* **2020**, *200*, 42–55. [[CrossRef](#)]
27. Di, Y.X.; Wang, Y.M. Local Structure-Property Correlation of Fe-Based Amorphous Alloys: Based on Minor Alloying Research. *Acta Metall. Sin.* **2020**, *56*, 1558–1568.
28. Li, K.H.; Ge, J.C.; Liu, S.N.; Fu, S.; Yin, Z.X.; Zhang, W.T.; Chen, G.X.; Wei, S.C.; Ji, H.; Feng, T.; et al. In situ scattering study of multiscale structural evolution during liquid–liquid phase transition in Mg-based metallic glasses. *Rare Met.* **2021**, *40*, 3107–3116. [[CrossRef](#)]
29. Hu, X.; Ge, J.; Liu, S.; Fu, S.; Wu, Z.; Feng, T.; Liu, D.; Wang, X.; Lan, S. Combustion mechanism of Fe-Nb-B-Y amorphous alloys with anomalous exothermic phenomena. *Acta Metall. Sin.* **2021**, *57*, 542–552.
30. Shin, S.S.; Kim, H.K.; Lee, J.C.; Park, I.M. Effect of Sub-T_g Annealing on the Corrosion Resistance of the Cu–Zr Amorphous Alloys. *Acta Metall. Sin. Engl. Lett.* **2018**, *31*, 273–280. [[CrossRef](#)]
31. Liang, D.; Liu, X.; Zhou, Y.; Wei, Y.; Wei, X.; Xu, G.; Shen, J. Effects of Annealing Below Glass Transition Temperature on the Wettability and Corrosion Performance of Fe-based Amorphous Coatings. *Acta Metall. Sin. Engl. Lett.* **2022**, *35*, 243–253. [[CrossRef](#)]
32. Ren, Y.; Babaie, E.; Bhaduri, S.B. Nanostructured amorphous magnesium phosphate/poly (lactic acid) composite coating for enhanced corrosion resistance and bioactivity of biodegradable AZ31 magnesium alloy. *Prog. Org. Coat.* **2018**, *118*, 1–8. [[CrossRef](#)]
33. Eivani, A.R.; Mehdizade, M.; Chabok, S.; Zhou, J. Applying multi-pass friction stir processing to refine the microstructure and enhance the strength, ductility and corrosion resistance of WE43 magnesium alloy. *J. Mater. Res. Technol.* **2021**, *12*, 1946–1957. [[CrossRef](#)]
34. Qiu, X.; Thompson, J.W.; Billinge, S.J. PDFgetX2: A GUI-driven program to obtain the pair distribution function from X-ray powder diffraction data. *J. Appl. Crystallogr.* **2004**, *37*, 678. [[CrossRef](#)]
35. Dong, W.; Ge, J.; Ke, Y.; Ying, H.; Zhu, L.; He, H.; Liu, S.; Lu, C.; Lan, S.; Almer, J.; et al. In-situ observation of an unusual phase transformation pathway with Guinier-Preston zone-like precipitates in Zr-based bulk metallic glasses. *J. Alloys Compd.* **2020**, *819*, 153049. [[CrossRef](#)]
36. Lan, S.; Guo, C.; Zhou, W.; Ren, Y.; Almer, J.; Pei, C.; Hahn, H.; Liu, C.T.; Feng, T.; Wang, X.L.; et al. Engineering medium-range order and polyamorphism in a nanostructured amorphous alloy. *Commun. Phys.* **2019**, *2*, 117. [[CrossRef](#)]
37. Chen, S.Q.; Hui, K.Z.; Dong, L.Z.; Li, Z.; Zhang, Q.H.; Gu, L.; Zhao, W.; Lan, S.; Ke, Y.; Shao, Y.; et al. Excellent long-term reactivity of inhomogeneous nanoscale Fe-based metallic glass in wastewater purification. *Sci. China Mater.* **2020**, *63*, 453–466. [[CrossRef](#)]
38. Yang, L.; Miller, M.K.; Wang, X.L.; Liu, C.T.; Stoica, A.D.; Ma, D.; Almer, J.; Shi, D. Metallic Glasses: Nanoscale Solute Partitioning in Bulk Metallic Glasses. *Adv. Mater.* **2009**, *21*, 305–308. [[CrossRef](#)]
39. Kelton, K.F. A new model for nucleation in bulk metallic glasses. *Philos. Mag. Lett.* **1998**, *77*, 337–344. [[CrossRef](#)]
40. Duparc, O.H. The Preston of the Guinier-Preston Zones. *Guinier. Metall. Mater. Trans.* **2010**, *41*, 1873. [[CrossRef](#)]
41. Oden, M.; Rogström, L.; Knutsson, A.; Ternner, M.R.; Hedström, P.; Almer, J.; Ilavsky, J. In situ small-angle x-ray scattering study of nanostructure evolution during decomposition of arc evaporated TiAlN coatings. *Appl. Phys. Lett.* **2009**, *94*, 053114. [[CrossRef](#)]
42. Ilavsky, J.; Jemian, P.R. Irena: Tool suite for modeling and analysis of small-angle scattering. *J. Appl. Crystallogr.* **2009**, *42*, 347–353. [[CrossRef](#)]
43. Gleiter, H. Nanoglasses: A New Kind of Noncrystalline Material and the Way to an Age of New Technologies? *Small* **2016**, *12*, 2225–2233. [[CrossRef](#)] [[PubMed](#)]
44. Debye, P.; Anderson, H.R., Jr.; Brumberger, H. Scattering by an Inhomogeneous Solid. II. The Correlation Function and Its Application. *J. Appl. Phys.* **1957**, *28*, 679–683. [[CrossRef](#)]
45. Fu, S.; Liu, S.; Ge, J.; Wang, J.; Ying, H.; Wu, S.; Yan, M.; Zhu, L.; Ke, Y.; Luan, J.; et al. In situ study on medium-range order evolution during the polyamorphous phase transition in a Pd-Ni-P nanostructured glass. *J. Mater. Sci. Technol.* **2022**, *125*, 145–156. [[CrossRef](#)]
46. Lan, S.; Blodgett, M.; Kelton, K.F.; Ma, J.L.; Fan, J.; Wang, X.L. Structural crossover in a supercooled metallic liquid and the link to a liquid-to-liquid phase transition. *Appl. Phys. Lett.* **2016**, *108*, 211907. [[CrossRef](#)]

47. Wessels, V.; Gangopadhyay, A.K.; Sahu, K.K.; Hyers, R.W.; Canepari, S.M.; Rogers, J.R.; Kramer, M.J.; Goldman, A.I.; Robinson, D.; Lee, J.W.; et al. Rapid chemical and topological ordering in supercooled liquid Cu₄₆Zr₅₄. *Phys. Rev. B* **2011**, *83*, 094116. [[CrossRef](#)]
48. Dong, W.; Wu, Z.; Ge, J.; Liu, S.; Lan, S.; Gilbert, E.P.; Ren, Y.; Ma, D.; Wang, X.L. In situ neutron scattering studies of a liquid–liquid phase transition in the supercooled liquid of a Zr–Cu–Al–Ag glass-forming alloy. *Appl. Phys. Lett.* **2021**, *118*, 191901. [[CrossRef](#)]
49. Lan, S.; Zhu, L.; Wu, Z.; Gu, L.; Zhang, Q.; Kong, H.; Liu, J.; Song, R.; Liu, S.; Sha, G.; et al. A medium-range structure motif linking amorphous and crystalline states. *Nat. Mater.* **2021**, *20*, 1347. [[CrossRef](#)]
50. Li, Z.; Yu, Q.; Zhang, C.; Liu, Y.; Liang, J.; Wang, D.; Zhou, F. Synergistic effect of hydrophobic film and porous MAO membrane containing alkynol inhibitor for enhanced corrosion resistance of magnesium alloy. *Surf. Coat. Technol.* **2019**, *357*, 515–525. [[CrossRef](#)]
51. Lopes, D.R.; Silva, C.L.; Soares, R.B.; Pereira, P.H.R.; Oliveira, A.C.; Figueiredo, R.B.; Langdon, T.G.; Lins, V.F. Cytotoxicity and Corrosion Behavior of Magnesium and Magnesium Alloys in Hank’s Solution after Processing by High-Pressure Torsion. *Adv. Eng. Mater.* **2019**, *21*, 1900391. [[CrossRef](#)]
52. Kaur, H.; Tian, R.; Roy, A.; McCrystall, M.; Horvath, D.V.; Lozano Onrubia, G.; Smith, R.; Ruether, M.; Griffin, A.; Backes, C.; et al. Correction to Production of Quasi-2D Platelets of Nonlayered Iron Pyrite (FeS₂) by Liquid-Phase Exfoliation for High Performance Battery Electrodes. *ACS Nano* **2021**, *14*, 13418–13432. [[CrossRef](#)]
53. Vladescu, A.; Pruna, V.; Kulesza, S.; Braic, V.; Titorencu, I.; Bramowicz, M.; Gozdziewska, A.; Parau, A.; Cotrut, C.M.; Pana, I.; et al. Influence of Ti, Zr or Nb carbide adhesion layers on the adhesion, corrosion resistance and cell proliferation of titania doped hydroxyapatite to the Ti6Al4V alloy substrate, utilizable for orthopaedic implants. *Ceram. Int.* **2018**, *45*, 1710–1723. [[CrossRef](#)]
54. Zhu, Y.B.; Shen, Z.C.; Zhnag, C.F.; Huang, D.P. *Electrochemical Data Manual*; Hunan Science & Technology Press: Changsha, China, 1985.
55. Zhang, Y.; Yan, C.; Wang, F.; Li, W. Electrochemical behavior of anodized Mg alloy AZ91D in chloride containing aqueous solution. *Corros. Sci.* **2005**, *47*, 2816–2831. [[CrossRef](#)]
56. McFeely, F.R.; Kowalczyk, S.P.; Ley, L.; Shirley, D.A. Multiplet splittings of the 4s and 5s core levels in the rare earth metals. *Phys. Lett. A* **1974**, *49*, 301–302. [[CrossRef](#)]
57. Soma, M.; Seyama, H. Surface compositions of powdered rock samples studied by X-ray photoelectron spectroscopy. *Chem. Geol.* **1986**, *55*, 97–103. [[CrossRef](#)]
58. Song, G. *Corrosion of Magnesium Alloys*; Woodhead Publishing Ltd.: Sawston, UK, 2011.
59. Zhang, Y.; Fang, Y.; Feng, S.; Ma, D.; Zhou, Y.; Wang, L.M. Trapping mechanism of metastable β-Ga disclosed by its lattice stability optimization and nucleation behavior exploration. *Calphad* **2022**, *79*, 102475. [[CrossRef](#)]
60. Li, Q. Formation of bulk ferromagnetic nanostructured Fe₄₀Ni₄₀P₁₄B₆ alloys by metastable liquid spinodal decomposition. *Sci. China Ser. E Technol. Sci.* **2009**, *52*, 1919–1922. [[CrossRef](#)]
61. Feng, S.; Qi, L.; Wang, L.; Pan, S.; Ma, M.; Zhang, X.; Li, G.; Liu, R. Atomic structure of shear bands in Cu₆₄Zr₃₆ metallic glasses studied by molecular dynamics simulations. *Acta Mater.* **2015**, *95*, 236–243. [[CrossRef](#)]
62. Xiang, S.; Li, Q.; Zuo, M.; Cao, D.; Li, H.; Sun, Y. Influence of the preparation cooling rate on crystallization kinetics of Fe₇₄Mo₆P₁₃C₇ amorphous alloys. *J. Non-Cryst. Solids* **2017**, *475*, 116–120. [[CrossRef](#)]